FOUR-DIMENSIONAL ELECTRICAL CAPACITANCE TOMOGRAPHY IMAGING USING EXPERIMENTAL DATA

M. Soleimani, C. N. Mitchell, and R. Banasiak

Electronic and Electrical Engineering
The University of Bath
Bath, UK

R. Wajman

Computer Engineering Department
Technical University of Lodz
Poland

A. Adler

Systems and Computer Engineering
Carleton University
Canada

Abstract—Electrical capacitance tomography (ECT) is a relatively mature non-invasive imaging technique that attempts to map dielectric permittivity of materials. ECT has become a promising monitoring technique in industrial process tomography especially in fast flow visualization. One of the most challenging tasks in further development of ECT for real applications are the computational aspects of the ECT imaging. Recently, 3D ECT has gained interest because of its potential to generate volumetric images. Computational time of image reconstruction in 3D ECT makes it more difficult for real time applications. In this paper, we present a robust and computationally efficient 4D image reconstruction algorithm applied to real ECT data. The method takes advantage of temporal correlation between 3D ECT frames to reconstruct movies 4D of dielectric maps. Image reconstruction results are presented for the proposed algorithms for experimental ECT data of a rapidly moving object.

Corresponding author: M. Soleimani (m.soleimani@bath.ac.uk).

1. INTRODUCTION

Electrical capacitance tomography (ECT) is a relatively mature imaging method in industrial process tomography [22, 23]. The aim of ECT is to image materials with a contrast in dielectric permittivity by measuring capacitance from a set of electrodes. Applications of ECT include the monitoring of oil-gas flows in pipelines, gas-solids flows in pneumatic conveying and imaging flames in combustion, gravitational flows in silo [10].

There has been a great deal of progress in image reconstruction methods, especially applied to 2D ECT; however, 3D ECT presents especially challenging numerical issues [8, 15, 17, 18, 20, 21]. 3D ECT is valuable for imaging the volumetric distribution of electrical permittivity. 3D ECT image reconstruction presents a similar inverse problem to electrical impedance tomography (EIT) which has been extensively studied, so ECT will naturally benefit from progress in EIT image reconstruction. Similar to EIT, Microwave tomography [17], ECT has potential to generate images with high temporal resolution and relatively poor spatial resolution. The spatial resolution is limited as a result of the inherent ill-posedness of the inverse problem and the existence of modeling and measurement errors and limited number of independent measurements. Various new and emerging imaging techniques, such as microwave imaging, acoustic imaging, optical imaging [2, 3, 5, 6, 14, 25] all lead to similar ill-posed inverse problems.

Some of early work in 3D ECT was shown [21] in which two and three-phase flow could be visualized using volumetric ECT. A Kalman filter based temporal image reconstruction has been presented in [16] using 2D ECT experimental data. Dynamic regularization method has been introduced earlier in [12, 13]. ECT image reconstruction is ill-conditioned, and is typically solved by adding a priori information using a regularized matrix $\mathbf{R}$, which represents underlying image probability distribution. Conventional single-step ECT reconstruction algorithms reconstruct each image from a single frame of data. This has two main disadvantages: first, since ECT data acquisition is typically more rapid than the underlying changes in the medium, successive data frames are correlated. Reconstruction of each data frame individually ignores this potentially useful source of information. Secondly, ECT data acquisition is inherently sequential, and the measurements which form a data frame are not all taken at the same instant. Failure to account for this fact may bias reconstructed images. The 4D algorithm creates movie images of electrical permittivity directly from multi-frame ECT data, so it is not a post processing 4D image reconstruction. Higher temporal resolution makes the ECT a good candidate for

4D imaging technique which is capable of monitoring on fast-varying industrial process applications.

2. EXPERIMENTAL SETUP

A typical three-dimensional capacitance sensor comprises an array of conducting plate electrodes, which are mounted on the outside of a non-conducting pipe, and surrounded by an electrical shield. For a metal wall pipe/vessel, the sensing electrodes must be mounted internally, with an insulation layer between the electrodes and the metal wall and using the metal wall as the electrical shield. Other components in the sensor include radial and axial guard electrodes, which are arranged differently to reduce the external coupling between the electrodes and to achieve improved quality of measurements and hence images. As usually the electrodes do not make physical contact with the materials to be measured, ECT provides a non-intrusive and non-invasive means, avoiding the risk of contamination.

In this paper, a 32-eletrodes ECT sensor has been introduced with 4 planes and 8 electrodes on each plane. The first and fourth plane consists of 58 mm of width and 70 mm of height copper plates. The planes in the middle consist of 58 mm of width and 30 mm of height copper plates. This approach improves an uniformity effective field of imaging for the whole volume of the sensor. A copper shield with a 15 mm distance from electrode array has been used for the screening purpose, a 32-channel ECT system called ET3 [9], has been applied. The numerical sensor simulation and the on-line 3D image reconstruction has been carried out using Matlab code, Visualization ToolKit (VTK) scientific visualization library (www.vtk.org) and Intel Xeon quad core based workstation with 16 GB of RAM. The electrode arrangement used in this study is 32 electrodes 3D ECT system that has been depicted in Figure 1.

3. FORWARD MODELLING

The forward problem is the simulation of measurement data for given value of excitation and material (permittivity) distribution and the inverse problem is the imaging result for a given set of measurement data. The inverse problem is formulated in terms of a minimization of errors based on the forward problem. Finite element method is well suited for the forward problem in 3D ECT, the application of boundary element method [24] could be potentially interesting, especially for shape reconstruction problem.

(a)

(b)
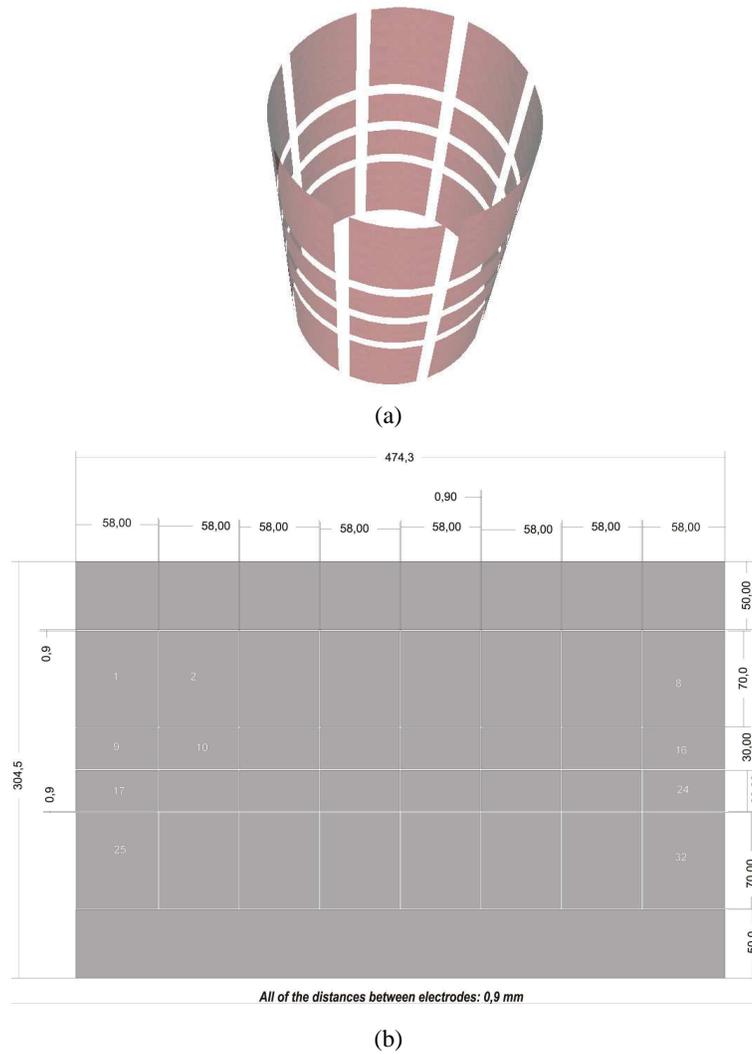
Figure 1. 32 electrodes array for 3D ECT system, (a) 4 planes with 8 electrodes in each plane, (b) PCB layout with dimensions used for sensor fabrication.

We use low frequency approximation to the Maxwell's equations. In a simplified mathematical model, the electrostatic approximation $\nabla \times E = 0$ is taken, effectively ignoring the effect of wave propagation. Let's take $E = -\nabla u$ and assume no internal charges. Then the

following equation holds.

$$\nabla \cdot (\varepsilon \nabla u) = 0 \quad \text{in} \quad \Omega \tag{1}$$

where u is the electric potential, ε is dielectric permittivity and Ω is the region containing the field. The potential on each electrode is known as

$$u = V_k \quad \text{on electrode } e_k \tag{2}$$

where e_k is the k-th electrode held at the potential V_k. Using finite element discretization of the Equation (1) using first order with the boundary condition (2) linear system of equations is obtained as

$$\mathbf{K}(\varepsilon)\mathbf{U} = \mathbf{B} \tag{3}$$

where the matrix $\mathbf{K}$ is the discrete representation of the operator $\nabla \cdot \varepsilon \nabla$ nd the vector $\mathbf{B}$ is the boundary condition term and $\mathbf{U}$ is the vector of electric potential solution. The total charge on the k-th electrode is given by

$$Q_k = \int_{E_k} \varepsilon \frac{\partial u}{\partial \hat{a}_n} dx^2 \tag{4}$$

where $\hat{a}_n$ is the inward normal on the k-th electrode, the surface integral of the Equation (3) is done over the surface of electrode (E_k) and the capacitance is calculated by $C = Q/V$. The Jacobian matrix $\mathbf{S}$ is calculated using an efficient method [15]. Each raw of the Jacobian matrix is the sensitivity of one measurement as a result of small change in each voxel in the imaging area. Another word, an element of the Jacobian matrix in the derivative of the measured capacitance at the boundary divided to the derivative of permittivity of a voxel [7]. An efficient formulation to calculate the Jacobian matrix uses the results of the forward problems and mutual energy concept to calculate the Jacobian matrix [4, 15]. The solution of the forward problem and the Jacobian matrix is used to solve the inverse problem, which is the estimation of the permittivity distribution given the measured capacitance data.

4. 4D INVERSION

Instead of calculating an image based on the sequence of past frames, we propose a temporal image reconstruction algorithm which uses a set of data frames nearby in time [1]. The data frame sequence is treated as a single inverse problem, with regularization prior to account for both spatial and temporal correlations between image elements. Figure 2 shows an schematic diagram for 4D imaging.
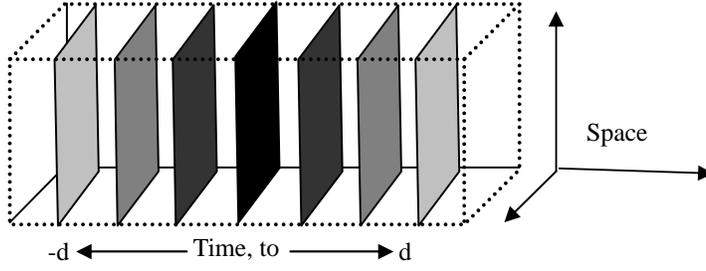
Figure 2. 4D ECT image reconstructions, each of the image slices in this demonstration is a 3D image frame, together with time we create a movie (4D).

Given a vertically concatenated sequence of capacitance measurements (normalized capacitance data) frames $\tilde{\mathbf{C}} = [\mathbf{C}_{-d}, \ldots, \mathbf{C}_0, \ldots, \mathbf{C}_d]$ and the corresponding relative permittivity images $\tilde{\varepsilon} = [\varepsilon_{-d}, \ldots, \varepsilon_0, \ldots, \varepsilon_d]$, the direct temporal forward model $\mathbf{C} = \mathbf{S}\varepsilon + \mathbf{n}$ is rewritten as

$$
\begin{bmatrix} \mathbf{C}_{-d} \\ \vdots \\ \mathbf{C}_0 \\ \vdots \\ \mathbf{C}_d \end{bmatrix} = \begin{bmatrix} \mathbf{S} & & \cdots & & 0 \\ & \ddots & & & \\ \vdots & & \mathbf{S} & & \vdots \\ & & & \ddots & \\ 0 & & \cdots & & \mathbf{S} \end{bmatrix} \begin{bmatrix} \varepsilon_{-d} \\ \vdots \\ \varepsilon_0 \\ \vdots \\ \varepsilon_d \end{bmatrix} + \begin{bmatrix} \mathbf{n}_{-d} \\ \vdots \\ \mathbf{n}_0 \\ \vdots \\ \mathbf{n}_d \end{bmatrix} \tag{5}
$$

and also as

$$
\tilde{\mathbf{C}} = \tilde{\mathbf{S}}\tilde{\varepsilon} + \tilde{\mathbf{n}} \tag{6}
$$

where $\tilde{\mathbf{n}} = [\mathbf{n}_{-d}; \ldots; \mathbf{n}_0; \ldots; \mathbf{n}_d]$ is the noise in the measured data. We assume $\mathbf{S}$ to be constant, although this formulation could be modified to account for a time variation in $\mathbf{S}$. Based on this approximation $\tilde{\mathbf{S}} = \mathbf{I} \otimes \mathbf{S}$, where the identity $\mathbf{I}$ has size $2d+1$, and $\otimes$ is the Kronecker product.

The correlation of corresponding elements between adjacent frames (delay $t = 1$) can be evaluated by an inter-frame correlation γ, which has value between 0 (independent) and 1 (fully dependent). As the frames become separated in time, the inter-frame correlation decreases; for an inter-frame separation t, the inter-frame correlation is γ^t. Frames with large time lag, $|t| > d$, can be considered independent. Image reconstruction is then defined in terms of minimizing the

augmented expression:

$$
\left\| \begin{bmatrix} \mathbf{C}_{-d} \\ \vdots \\ \mathbf{C}_0 \\ \vdots \\ \mathbf{C}_d \end{bmatrix} - \begin{bmatrix} \mathbf{S} & \cdots & & \mathbf{0} \\ & \ddots & & \\ \vdots & & \mathbf{S} & & \vdots \\ & & & \ddots & \\ \mathbf{0} & \cdots & & \mathbf{S} \end{bmatrix} \begin{bmatrix} \varepsilon_{-d} \\ \vdots \\ \varepsilon_0 \\ \vdots \\ \varepsilon_d \end{bmatrix} \right\|_{\tilde{\mathbf{W}}}^{\mathbf{2}} + \lambda^{\mathbf{2}} \left\| \begin{bmatrix} \varepsilon_{-d} \\ \vdots \\ \varepsilon_0 \\ \vdots \\ \varepsilon_d \end{bmatrix} \right\|_{\tilde{\mathbf{R}}}^{2}
\tag{7}
$$

and the inversion can be written as

$$
\tilde{\mathbf{B}} = \tilde{\mathbf{R}}^{-1}\tilde{\mathbf{S}}^{\mathbf{T}}(\tilde{\mathbf{S}}\tilde{\mathbf{R}}^{-1}\tilde{\mathbf{S}}^{\mathbf{T}} + \lambda^2 \tilde{\mathbf{W}}^{-1})^{-1}
\tag{8}
$$

where $\tilde{\mathbf{W}} = \mathbf{I} \otimes \mathbf{W}$ and $\mathbf{W}$ is regularization matrix for the measurement noise (in context of Tikhonov regularization, $\mathbf{W} = \sigma_n^2 \sum_n^{-1}$, where σ_n is the average measurement noise), $\tilde{\mathbf{W}}$ is diagonal since measurement noise is uncorrelated between frames. This paper uses model, $\mathbf{W} = \mathbf{I}$. Here λ is the regularization parameter. $\tilde{\mathbf{R}} = \Gamma^{-1} \otimes \mathbf{R}$, $\mathbf{R}$ is the regularization matrix ($\mathbf{R} = \sigma_\varepsilon \sum_\varepsilon^{-1}$ where σ_ε is *a priori* amplitude of permittivity changes and $\tilde{\mathbf{R}}$ includes the temporal and spatial changes of permttivity) that represents the spatial correlations between image voxels (The regularization matrix $\mathbf{R}$ may be understood to model the "unlikelihood" of image element configurations) and Γ is the temporal weight matrix of an image sequence $\tilde{\varepsilon}$ and is defined to have the form as

$$
\Gamma = \begin{bmatrix} 1 & \gamma & \cdots & \gamma^{2d-1} & \gamma^{2d} \\ \gamma & 1 & \cdots & \gamma^{2d-2} & \gamma^{2d-1} \\ \vdots & \vdots & \ddots & \vdots & \vdots \\ \gamma^{2d-1} & \gamma^{2d-2} & \cdots & 1 & \gamma \\ \gamma^{2d} & \gamma^{2d-1} & \cdots & \gamma & 1 \end{bmatrix}
\tag{9}
$$

From (8) and (9),

$$
\tilde{\mathbf{B}} = \left[\mathbf{\Gamma} \otimes \left(\mathbf{P}\mathbf{S}^{\mathbf{T}} \right) \right] \cdot \left[\mathbf{\Gamma} \otimes \left(\mathbf{S}\mathbf{P}\mathbf{S}^{\mathbf{T}} \right) + \lambda^2 \left(\mathbf{I} \otimes \mathbf{V} \right) \right]^{-1}
\tag{10}
$$

where $\mathbf{P} = \mathbf{R}^{-1}$ and $\mathbf{V} = \mathbf{W}^{-1}$. In practice, $\mathbf{P}$ and $\mathbf{V}$ are modeled directly from the system covariances, rather than the inverse of $\mathbf{R}$ and

W. 4D image can be reconstructed as

$$\begin{bmatrix} \tilde{\varepsilon}_{-d} \\ \vdots \\ \tilde{\varepsilon}_0 \\ \vdots \\ \tilde{\varepsilon}_d \end{bmatrix} = \tilde{\mathbf{B}}\tilde{\mathbf{C}} \tag{11}$$

Although this estimate is an augmented image sequence, we are typically only interested in the current image $\tilde{\varepsilon}_0$. It is calculated by $\tilde{\varepsilon}_0 = \hat{\mathbf{B}}_0 \tilde{\mathbf{C}}$ where $\hat{\mathbf{B}}_0$ is the rows $\mathbf{n_M d + 1} \ldots \mathbf{n_M} \times (\mathbf{d + 1})$ of $\tilde{\mathbf{B}}$, where $\mathbf{n_M}$ is number of measurements, in this paper for 32 electrodes ECT system $\mathbf{n_M} = 496$. It can be seen that the inversion formulation of the 4D ECT has the size of the number of measurement rather than number of voxels.

This will directly generate a 4D (movie) of the ECT image. If one wants to update the Jacobian and dynamically select the regularization parameters, then the calculation of $\tilde{\mathbf{B}}$ needs be done in each iteration of the 4D algorithm (each time that we have a new ECT data set). If we select a sigle set of regularization parameter and accept linear inverse problem the calculation of $\tilde{\mathbf{B}}$ can be done offline so the 4D algorithm becomes very fast.

If *a priori* knowledge of temporal change in permittivity is available (this could be developed by a physical model, i.e., fluid dynamic model for flow visualization), then we can select an optimal value for temporal correlation parameter. The γ is a parameter of the system; it depends on the data acquisition frame rate, the speed of underlying permittivity changes and the noise level in measurement system. A method to estimate the value of γ from measurement sequence will be resented here. By taking covariance on both sides of (6), we have the estimated covariance matrix of the data as

$$\hat{\sum}_{\tilde{C}} = \tilde{S}\sum_{\tilde{\varepsilon}}\tilde{S}^t + \sum_{\tilde{n}} \tag{12}$$

the optimal γ is chosen so that the error between the true data covariance matrix $\sum_{\tilde{C}}$ and the estimated one $\hat{\sum}_{\tilde{C}}$ is minimized as

$$\gamma = \arg\min_{\gamma} \left\| \sum_{\tilde{C}} - \sum_{\tilde{n}} - \tilde{S}\sum_{\tilde{\varepsilon}}\tilde{S}^t \right\|_F^2 \tag{13}$$

where subscript F is a matrix norm (Euclidean norm). Since $\sum_{\tilde{\varepsilon}} =$

$\Gamma \otimes \sum_{\varepsilon}$ and $\tilde{S} = I \otimes S$, (13) becomes

$$\gamma = \arg\min_{\gamma} \left\| \sum_{\tilde{C}} - \sum_{\tilde{n}} - \Gamma \otimes \left(S \sum_{\varepsilon} S^t \right) \right\|_F^2 \tag{14}$$

By taking covariance on both sides of $\mathbf{C} = \mathbf{S}\varepsilon + \mathbf{n}$, we have

$$\sum_C = S \sum_{\varepsilon} S^t + \sum_n \tag{15}$$

so that $S \sum_{\varepsilon} S^t = \sum_C - \sum_n$; we also have $\sum_{\tilde{n}} = I \otimes \sum_n$ and $\sum_{\tilde{C}} = \Gamma_C \otimes \sum_C$, where $\Gamma_C \in R^{(2d+1)\times(2d+1)}$ is the correlation matrix of $\tilde{C}$. Thus the optimal γ is calculated by

$$\gamma = \arg\min_{\gamma} \left\| \Gamma_C \otimes \sum_C - I \otimes \sum_n - \Gamma \otimes \left(\sum_C - \sum_n \right) \right\|_F^2 \tag{16}$$

Γ_C and $\sum_C$ can be calculated directly from the data. $\sum_n$ can be measured by calibration of ECT system. For computational efficiency, (16) can be simplified as

$$\gamma = \arg\min_{\gamma} \left\| \Gamma_C \left\| \sum_C \right\|_F^2 - I \left\| \sum_n \right\|_F^2 - \Gamma \left\| \sum_C - \sum_n \right\|_F^2 \right\|_F^2 \tag{17}$$

where Γ_C, $\|\sum_C\|_F^2$, $\|\sum_n\|_F^2$ and $\|\sum_C - \sum_n\|_F^2$ may be precalculated. Since Γ is relatively small ($R^{(2d+1)\times(2d+1)}$) this optimization can be performed directly by bisection search between limits. Assuming linear image reconstruction of Equation (15) enabled us to develop an estimation of temporal parameter in Equation (17) that only depends on covariance related to the measurement. An estimation method that takes into account nonlinearly between data and image (dynamical image here) is beyond scope of this paper.

5. EXPERIMENTAL RESULTS

In order to evaluate the performance of proposed method compared to traditional single step Gauss-Newton (but uncorrelated, here we call it 3D), synthetic data was generated using the same mesh. Spherical inclusion with permittivity 1.6 and radius 2.5 cm was centred in 7 different places starting from the corner (1 cm from the electrodes) to the centre of the imaging area with the 2 cm steps. The synthetically data was generated using a same mesh and up to 6% noise was added to the measure data. The percentage of random Gaussian noise was selected with respect to the average value of all measured capacitances.
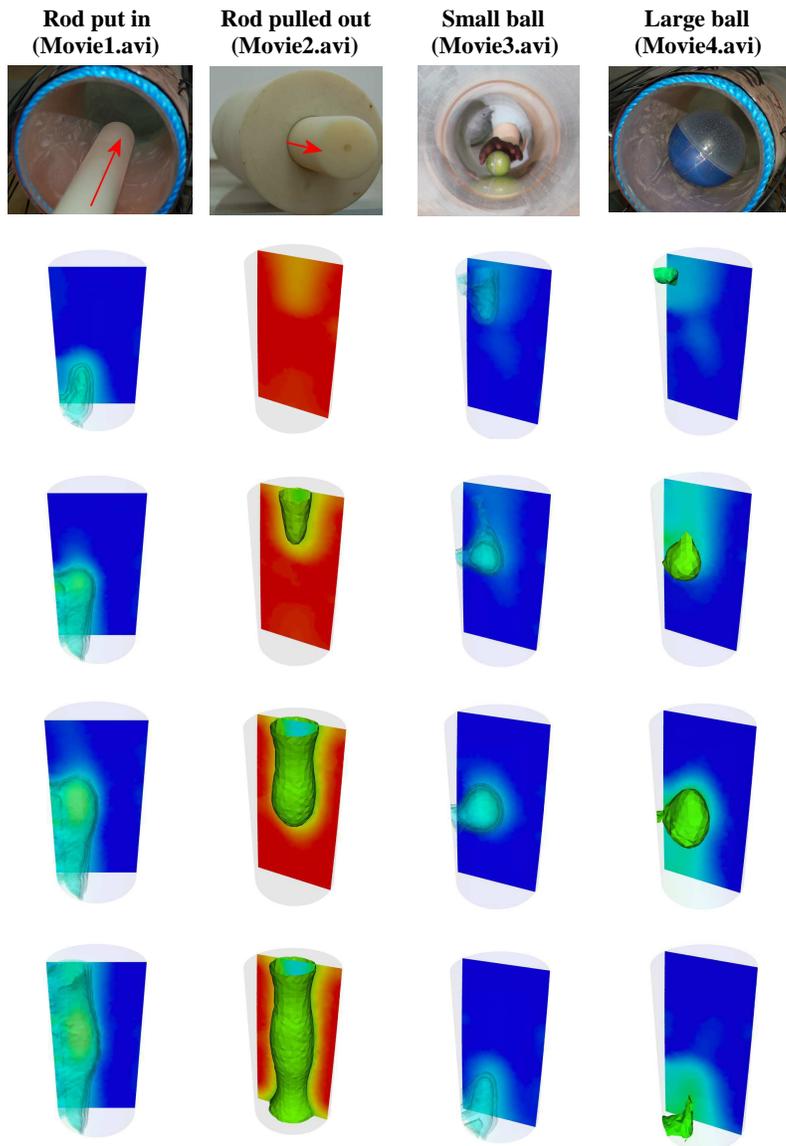
This figure shows superiority of the temporal image reconstruction with the high noise data. We repeated the same test with 0% and 2%, 3% and 6% added noise and Figure 3 shows the norm of the error between reconstructions in all three noise levels. Assuming ε_{tru} is true permittivity and ε_{rec} is reconstructed permittivity, the image error is defined as $\frac{\|\varepsilon_{true}-\varepsilon_{rec}\|}{\|\varepsilon_{true}\|}$. Temporal method works similar to the linear (temporally uncorrelated method) for noise free data and outperforms the linear uncorrelated algorithm (3D) in higher noise levels, suggesting a better noise performance. In all simulated and experimental results we select $tw = 0.8$ and $\lambda^2 = 10^{-4}$. These are seleced imperically in this study based on the fact that they produce satisfactory results. In real life applications (say for multi-phase flow application) these parameters has to be selected based on the physical reality of the experimental condition.

The proposed algorithm has been tested against several experimental example of moving 3D objects (4D). Figure 4 shows the reconstructed images for different moving objects in a tank. The movie includes several frames; here we only show few frames of the movie. The results presented in Figure 4 are among the first experimental results from proposed algorithm. In all cases 4D algorithms successfully reconstructed the movement of 3D object. The algorithm were also applied to two more experimental examples, similar results were observed in capturing dynamic of a moving 3D object (i.e., plastic rod) — see Figure 4. We have attached to this paper the movies related to each of these 4 experiments.

During the first two experiments we were using a cylindrical object with 150 mm of diameter and a concentrically drilled hole with 50 mm of diameter and a rod of the same diameter respectively. The cylinder and the rod both had been made from Ertalon with relative permittivity of about 3.2. Firstly the rod was being put with a constant velocity of about 2 cm/s near the wall of pipe. The rod was being pulled out from the bigger cylinder as the next experiment. The velocity of rod movement has been well-matched to the measurement abilities of used ET3 system which is now able to measure data in 32 channel mode with up to 15 frames per second [9]. It can be observed that 4D algorithm allows for on-line visualization of such objects in the whole volume of the sensor. In the next two experiments we moved two balls inside a pipe. The first ball was about 70 mm in diameter and the second one was bout 100 mm in diameter both filled with plastic granulate (relative permittivity of 2.6). We let these balls move freely through the pipe with constant velocity acquiring measurement data simultaneously. The results we have got using 4D algorithm are promising even though the velocity of balls was too high. It
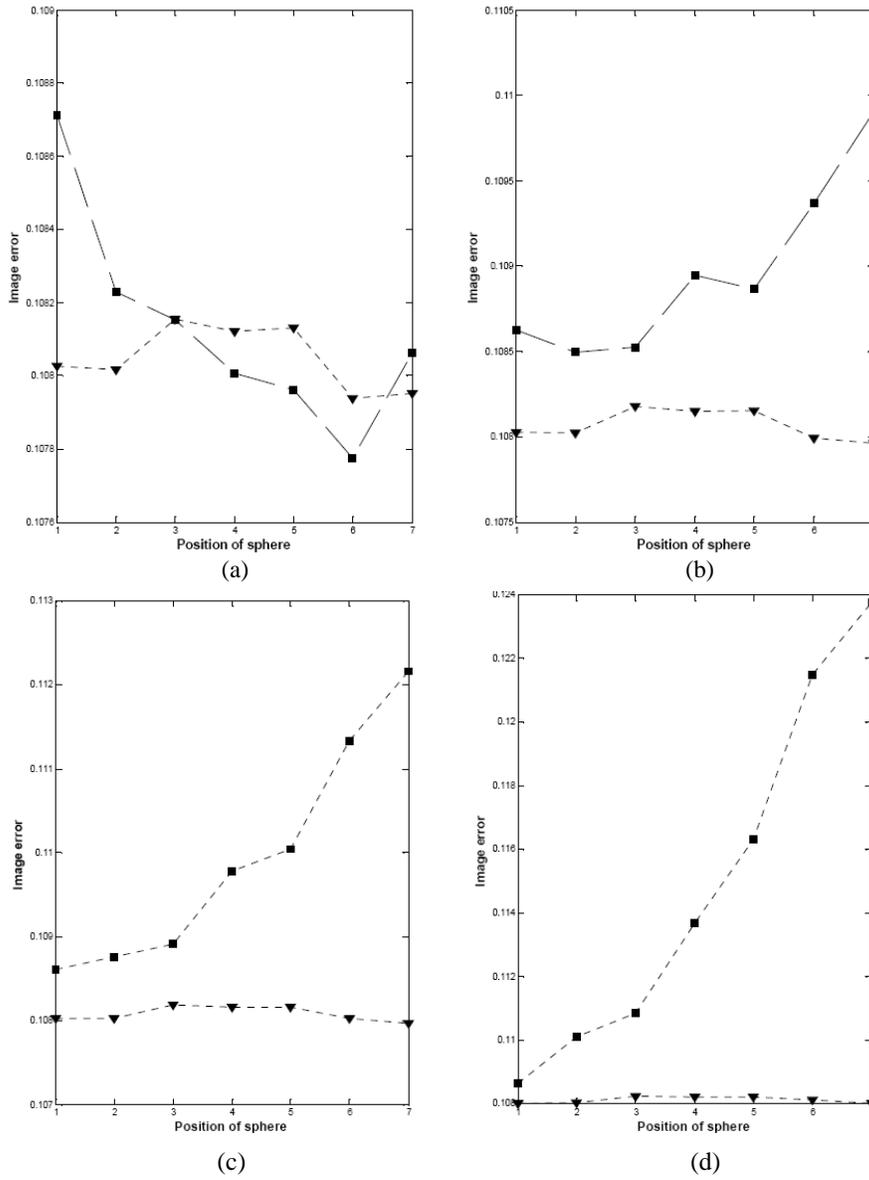
Figure 3. The error between simulated and real images using 3D (square) and 4D (triangle) methods (a): Noise free, (b): 2 percent noise, (c): 3 percent noise, (d): 6 percent noise.

Rod put in
(Movie1.avi)   **Rod pulled out**
(Movie2.avi)   **Small ball**
(Movie3.avi)   **Large ball**
(Movie4.avi)

Figure 4. 4D ECT visualisation of moving objects: for each case the image is a snap shot of 4D movie reconstruction for frames 45, 55, 135, 185 out of 200 frames in each case.

can be easily observed that some axial resolution limitations of a 3D capacitance sensor in the lower and upper part of the imaging volume exist which is obvious because of sensor coverage. The central area of the sensor volume characterizes relatively low sensitivity. Nevertheless the ball movement in that area has been visualized with acceptable quality regardless of poor sensitivity. The main bottleneck in these experiments we had to face with was the ET3 capacitance system which is now relatively slow in 32 channel mode. With faster and less noisy ECT system the quality of 4D images for on-line visualization would be improved. In order to implement a temporal solver in an ECT system for real-time imaging, a delay must be introduced between the measurements and reconstruction to allow acquisition of d "future frames". This corresponds to the linear phase filters used in digital signal processing applications. For fast ECT systems, with frame rates of for example 15 frames/sec, a choice of $d = 3$, introduces a delay 200 ms.

6. CONCLUSION

A direct temporal image reconstruction has been applied to the ECT that simultaneously reconstructs 4D dielectric permittivity imaging using multi-frame ECT data. Including a temporal correlation term and reconstruction of the 4D ECT images simultaneously improves the noise fidelity of the image reconstruction. We anticipate that the 4D algorithm could potentially improve the spatial resolution of ECT imaging. Study of improvement in image resolution using the 4D method is under way. The efficient implementation of the 4D algorithm is a promising aspect of the method presented here and with further work we are hoping to achieve a fully real time 4D reconstruction in ECT, which will pave the way for many more industrial applications for the ECT. Selection of the temporal hyperparameter depends on the data acquisition frame rate, the speed of underlying permittivity changes and the system noise level. Selection of spatial hyperparameter depends on the noise level in ECT system and a priori knowledge of the spatial distribution of the permittivity map. Our proposed future study is to use the 4D ECT for multi-phase flow visualization. A computational fluid dynamic (CFD) model will be used together with the ECT measurement data. The CFD model will provide physically meaningful information regarding the spatial distribution and dynamical changes of the flow. Combining this physical model within 4D ECT image reconstruction will enable us to select better functions and optimal parameters for temporal and spatial regularization. A similar work in context of the Kalman filter

has been studied earlier [11] and proved to be very promising. Better noise immunity achieved in proposed 4D algorithm is an opportunity to develop ECT sensor with larger number of electrodes, this in turn can improve the spatial resolution of the imaging technique.

REFERENCES

1. Adler, A., T. Dai, and W. R. B. Lionheart, "Temporal image reconstruction in electrical impedance tomography," *Physiol. Meas.*, Vol. 28, S1–S11, 2007.
2. Chen, G. P., W. B. Yu, Z. Q. Zhao, Z. P. Nie, and Q. H. Liu, "The prototype of microwave-induced thermo-acoustic tomography imaging by time reversal mirror," *Journal of Electromagnetic Waves and Applications*, Vol. 22, No. 11–12, 1565–1574, 2008.
3. Cheng, X. X., B. I. Wu, H. Chen, and J. A. Kong, "Imaging of objects through lossy layer with defects," *Progress In Electromagnetics Research*, PIER 84, 11–26, 2008.
4. Li, Y. and W. Q. Yang, "Image reconstruction by nonlinear Landweber iteration for complicated distributions," *Meas. Sci. Technol.*, Vol. 19, 094014 (8pp), 2008.
5. Huang, C. H., Y. F. Chen, and C. C. Chiu, "Permittivity distribution reconstruction of dielectric objects by a cascaded method," *Journal of Electromagnetic Waves and Applications*, Vol. 21, No. 2, 145–159, 2007.
6. Franceschini, G., M. Donelli, D. Franceschini, M. Benedetti, P. Rocca, and A. Massa, "Microwave imaging from amplitude-only data-advantages and open problems of a two-step multi-resolution strategy," *Progress In Electromagnetics Research*, PIER 83, 397–412, 2008.
7. Marashdeh, Q., W. Warsito, L. S. Fan, and F. L. Teixeira, "A nonlinear image reconstruction technique for ECT using a combined neural network approach," *Meas. Sci. Technol.*, Vol. 17, No. 8, 2097–2103, 2006.
8. Nurge, M. A., "Electrical capacitance volume tomography with high contrast dielectrics using a cuboid sensor geometry," *Meas. Sci. Technol.*, Vol. 18, No. 5, 1511–1520, 2007.
9. Olszewski, T., P. Brzeski, J. Mirkowski, A. Pląskowski, W. Smolik, and R. Szabatin, "Modular capacitance tomograph," *Proc. 4th International Symposium on Process Tomography in Warsaw*, 2006.
10. Romanowski, A., K. Grudzien, R. Banasiak, R. A. Williams, and D. Sankowski, "Hopper flow measurement data visualization:

Developments towards 3D," *Proc. 5th World Congress on Industrial Process Tomography*, Bergen, Norway, 2006.

11. Seppanen, A., M. Vauhkonen, P. Vauhkonen, E. Somersalo, and J. P. Kaipio, "Fluid dynamical models and state estimation in process tomography: Effect due to inaccuracies in flow fields," *Journal of Electronic Imaging*, Vol. 10, No. 3, 630–640, 2001.

12. Schmitt, U. and A. K. Louis, "Efficient algorithms for the regularization of dynamic inverse problems — Part I: Theory," *Inverse Problems*, Vol. 18, 645–658, 2002.

13. Schmitt, U., A. K. Louis, C. H. Wolters, and M. Vauhkonen, "Efficient algorithms for the regularization of dynamic inverse problems: II. Applications," *Inverse Problems*, Vol. 18, No. 1, 659–676, 2002.

14. Serdyuk, V. M., "Dielectric study of bound water in grain at radio and microwave frequencies," *Progress In Electromagnetics Research*, PIER 84, 379–406, 2008.

15. Soleimani, M., "Three-dimensional electrical capacitance tomography imaging," *Insight, Non-destructive Testing and Condition Monitoring*, Vol. 48, No. 10, 613–617, 2006.

16. Soleimani, M., M. Vauhkonen, W. Q. Yang, A. J. Peyton, B. S. Kim, and X. Ma, "Dynamic imaging in electrical capacitance tomography and electromagnetic induction tomography using a Kalman filter," *Meas. Sci. Tech.*, Vol. 18, No. 11, 3287–3294, 2007.

17. Soleimani, M., H. Wang, Y. Li, and W. Yang, "A comparative study of three dimensional electrical capacitance tomography," *International Journal for Information Systems Sciences*, Vol. 3, No. 2, 283–291, 2007.

18. Wajman, R., R. Banasiak, L. Mazurkiewicz, D. Dyakowski, and D. Sankowski, "Spatial imaging with 3D capacitance measurements," *Meas. Sci. Technol.*, Vol. 17, No. 8, 2113–2118, 2006.

19. Warsito, W., Q. Marashdeh, and L. S. Fan, "Electrical capacitance volume tomography," *IEEE Sensors Journal*, Vol. 7, No. 3–4, 525–535, 2007.

20. Warsito, W. and L.-S. Fan, "Development of 3-dimensional electrical capacitance tomography based on neural network multi-criterion optimization image reconstruction," *Proc. 3rd World Congress on Industrial Process Tomography (Banff)*, 942–947, 2003.

21. Warsito, W. and L. S. Fang, "Imaging the bubble behavior using the 3-D electric capacitance tomograph," *Chem. Eng. Sci.*, Vol. 60,

No. 22, 6073–6084, 2005.

22. Yang, W. Q., "Key issues in designing capacitance tomography sensors," *IEEE Conference on Sensors*, 497–505, Daegu, Korea, October 22–25, 2006.

23. Yang, W. Q. and G. L. Pen, "Review of image reconstruction algorithms for electrical capacitance tomography, Part 1: Principles," *Proc. International Symposium on Process Tomography in Poland (Wroclaw)*, 123–132, 2002.

24. Zacharopoulos, A. and S. Arridge, "3D shape reconstruction in optical tomography using spherical harmonics and BEM," *Journal of Electromagnetic Waves and Applications*, Vol. 20, No. 13, 1827–1836, 2006.

25. Zhong, X. M., C. Liao, W. Chen, Z. B. Yang, Y. Liao, and F. B. Meng, "Image reconstruction of arbitrary cross section conducting cylinder using UWB pulse," *Journal of Electromagnetic Waves and Applications*, Vol. 21, No. 1, 25–34, 2007.